Frontiers in Sustainable Cities

METHODS
published: 22 July 2022
doi: 10.3389/frsc.2022.869743

Resolving Radiant: Combining Spatially Resolved Longwave and Shortwave Measurements to Improve the Understanding of Radiant Heat Flux Reflections and Heterogeneity

Coleman Merchant[1]*, Forrest Meggers[1]*, Miaomiao Hou[2,3], Dorit Aviv[2], Florian Arwed Schneider[4] and Ariane Middel[5,6]

[1] Princeton School of Architecture and the Andlinger Center for Energy and the Environment, Princeton University, Princeton, NJ, United States, [2] Weitzman School of Design, University of Pennsylvania, Philadelphia, PA, United States, [3] College of Architecture and Urban Planning, Tongji University, Shanghai, China, [4] School of Sustainability, Arizona State University, Tempe, AZ, United States, [5] School of Arts, Media and Engineering, Arizona State University, Tempe, AZ, United States, [6] School of Computing and Augmented Intelligence, Arizona State University, Tempe, AZ, United States

Edited by:
Jennifer Ann Salmond,
The University of Auckland,
New Zealand

Reviewed by:
Dahai Qi,
Université de Sherbrooke, Canada
Xiangfei Kong,
Hebei University of Technology, China

***Correspondence:**
Coleman Merchant
cbm5@princeton.edu
Forrest Meggers
fmeggers@princeton.edu

Specialty section:
This article was submitted to
Health and Cities,
a section of the journal
Frontiers in Sustainable Cities

Received: 04 February 2022
Accepted: 17 May 2022
Published: 22 July 2022

Citation:
Merchant C, Meggers F, Hou M, Aviv D, Schneider FA and Middel A (2022) Resolving Radiant: Combining Spatially Resolved Longwave and Shortwave Measurements to Improve the Understanding of Radiant Heat Flux Reflections and Heterogeneity. Front. Sustain. Cities 4:869743. doi: 10.3389/frsc.2022.869743

We introduce and demonstrate new measurement and modeling techniques to fully resolve the spatial variation in shortwave and longwave radiant heat transfer in the outdoor environment. We demonstrate for the first time a way to directly resolve the shortwave radiant heat transfer from terrestrial reflected and diffuse sky components along with the standard direct solar radiation using an adapted thermopile array and ray-tracing modeling techniques validated by 6-direction net radiometer. Radiant heat transfer is a major component of heat experienced in cities. It has significant spatial variability that is most easily noticed as one moves between shade and direct solar exposure. But even on a cloudy and warm day the invisible longwave infrared thermal radiation from warm surfaces makes up a larger fraction of heat experienced than that caused by convection with surrounding air. Under warm or hot climate conditions in cities, radiant heat transfer generally accounts for the majority of heat transfer to people. Both the shortwave (visible/solar) and the longwave (infrared/thermal) have significant spatial variation. We demonstrate sensor methods and data analysis techniques to resolve how these radiant fluxes can change the heat experienced by >1 kWm^{-2} across small distances. The intense solar shortwave radiation is easily recognized outdoors, but longwave is often considered negligible. Longwave radiation from heat stored in urban surfaces is more insidious as it can cause changes invisible to the eye. We show how it changes heat experienced by >200 Wm^{-2}. These variations are very common and also occur at the scale of a few meters.

Keywords: radiant heat transfer, thermal sensors, urban heat, longwave, shortwave, thermopile array

INTRODUCTION AND BACKGROUND

The measurement of heat impacts on people in the built environment is critical to understanding and addressing issues of human health, climate, and urban design. Climate change is increasing average temperatures across the globe, with the most recent Intergovernmental Panel on Climate Change (IPCC) assessment reporting a higher average temperature increase across the last century of 1.59°C over land compared to ocean, and additionally stating that cities will intensify human-induced warming locally (IPCC, 2021). Heat is also increasing even more in urban areas due to radiative trapping and anthropogenic emissions of heat (Oke, 1982). These temperature increases all represent surface air temperatures. As we and others have shown, surface temperatures can easily be >30°C warmer than air temperatures reaching extremes above 60°C (Yang and Li, 2015; Meggers et al., 2016; Middel and Krayenhoff, 2019; Aviv et al., 2021). We argue that the direct radiant heat transfer from these hot surfaces not only add to the heat experienced from warmer urban air temperatures, but actually have significantly larger impacts than the warmer air on urban dwellers. In this paper we will demonstrate new techniques that produce novel results describing the complex longwave, shortwave, and reflecting components of radiant heat transfer as it bounces through the urban environment independent of air temperature.

The general population largely associates heat with air temperatures, but in warm climates the majority of heat experienced by people in the urban environment is in the form of radiant heat transfer (Hoppe, 1992; Thorsson et al., 2007; Johansson et al., 2014; Middel et al., 2014; Lindberg et al., 2016). We have built human body heat models (Teitelbaum et al., 2020), and built experimental radiant pavilions (Chen et al., 2020; Teitelbaum et al., 2022), which have both demonstrated how as air temperatures approach skin temperature the body's necessary metabolic heat rejection can become almost completely dependent on radiant heat heat transfer. We argue it is therefore critical to explore new ways to model and measure radiant heat transfer that include its complex geometric and spectral properties.

Background

Radiant heat transfer is the exchange of heat by the emission and absorption of electromagnetic radiation between surfaces. Governed by blackbody radiation physics described by Planck, the temperature of surfaces drives the emission of thermal radiation, including between people and their surroundings. Radiant heat transfer occurs across the full spectrum of radiation, and as the emission is related to temperatures there are two dominant modes of radiant heat experienced: solar shortwave radiation and terrestrial longwave radiation. The sun, at around 5000 K, emits shortwave light peeking around 0.5–1 micron wavelengths that we have evolved to see with our eyes, but that also brings around 1 kWm^{-2} to the surface of the Earth. The Earth, including those of us existing on it, are only around 300K and therefore emit largely in the longwave wavelengths of 8–15 micron, creating a dynamic exchange between surfaces on the planet that is invisible to the human eye.

For shortwave radiation there is an intuitive association of heat felt from the intense solar direct beam, and an understanding that black materials (low albedo and heat absorption) will absorb more of this heat than white materials (high albedo and heat reflection). The longwave radiation is not visible to the human eye and it is not transmitted via an intense direct beam, but rather is diffusely emitted and exchanged between surfaces, which makes the view factor to surrounding surfaces and their varying temperatures critical in understanding radiant heat impacts. While finding shade from the sun is an obvious strategy to reduce radiant heat, it is nearly impossible for a human to adapt to the diffuse longwave heat surrounding them in the urban environment. In addition, even in the shade the diffuse shortwave radiation that diffusely reflects off high-albedo surfaces is also non-trivial.

In this paper we build on previous work that strives to better characterize the invisible longwave radiant heat along with the shortwave components coming from all directions. As demonstrated by the work of the mobile human-biometeorological station (MaRTy cart) experimentally in previous work at Arizona State University (ASU) in Tempe, Arizona (Middel and Krayenhoff, 2019), we can measure precisely the longwave and shortwave radiation using the 6-direction net radiometer setup, and move through a variety of locations demonstrating that lateral longwave and shortwave radiation dominate heat experienced with invisible longwave being the dominant flux. This work showed that MRT reached above 75°C, and that these sites were above asphalt or concrete. It also demonstrated the benefits of green surfaces like trees in reducing sky view factor and Mean Radiant Temperature (MRT). The 6-direction radiometer method provides averaged directional readings of the Wm^{-2} of radiation, but does not resolve the specific surfaces. In previous work at Princeton the Spherical Motion Average Radiant Temperature (SMaRT) sensor was developed to scan and map longwave radiant heat emission from surfaces with a high resolution thermal array, which enabled analysis of the exact sources of radiant heat and resolving the exact location of hot surfaces and their geometry relative to potential occupants in space (Teitelbaum et al., 2016, 2017; Houchois et al., 2019). With this work we were able to show how radiant heat can vary significantly across surfaces, and also to calculate the distribution of MRT at any point in space as a function of the highly resolved surrounding surface temperatures and geometries measured by the sensor. This showed that indoor surfaces often varied by more than 10°C and MRT could vary by > 2°C when moving just 2 feet (60 cm) in a standard heated office. The Princeton and ASU team initially brought the MaRTy cart and the SMaRT sensor platforms together to explore potential methods combining the high precision and high resolution aspects of each system in a 1-day experimental campaign in Philadelphia on the Temple University campus (Aviv et al., 2021). As there were gaps in data produced by the systems, a simulation technique was added from collaborators at Penn that was informed by the results from both systems to create spatial characterizations of the urban environment that built on previous ray tracing techniques for longwave heat transfer (Aviv, 2019; Aviv et al., 2022). The modeling techniques became integrated as a tool for data reduction and analysis from the two sensor platforms, which helped to generate results that created a data-driven mapping of varying MRT throughout an outdoor space in the collaborative paper that showed for the first time a method to combine high resolution surface temperatures showing variations in MRT in space that could be validated against precise net radiometer measurements (Aviv et al., 2021).

The measurement and modeling of shortwave are both improved in this paper. Modeling the radiative exchanges on and within urban surfaces can be done several ways. Some studies on urban climate have integrated ray tracing techniques into the urban canopy model. A neighborhood-scale multi-layer urban canopy model (MUCM) combined with ray tracing methods was developed to account for shortwave and longwave radiation exchange in the urban canyon, but it is based on the two-dimensional canyon geometry and thus not feasible to use a detailed three-dimensional geometry model as the input (Krayenhoff et al., 2013). Doan and Kusaka (2019) introduced a new MUCM also combined with a ray-tracing algorithm to represent both shortwave and longwave radiative processes on urban surfaces. The urban geometry model considers buildings and vegetation land as bulks with thermal properties. Based on the urban canyon model, Rosado et al. (2017) proposed an urban canyon albedo model (UCAM) to calculate the amount of radiant flux accounting for three reflection bounces, and the results demonstrated the need to use the actual urban geometry for more accurate studies. Another approach is using a ray tracing model directly. A three-dimensional numerical model based on ray tracing methods was developed by Yang and Li (2015) to predict a detailed urban surface temperature distribution. The urban geometry model consists of normalized cells, representing different abstracted scenarios of building density, height and arrangements. The aforementioned work took reflection and urban albedo as important parameters when testing different scenarios. There are also studies investigating the influence of shortwave reflections on the energy balance (Vallati et al., 2018; Ali-Toudert, 2021). As an approach that can support detailed urban geometry model, the solar and longwave environmental irradiance geometry (SOLWEIG) model can simulate spatial variations of three-dimensional radiation fluxes in complex urban settings with building digital elevation model as input (Lindberg et al., 2008; Lindberg and Grimmond, 2011) and has been tested in cases of different cities. For example, Chen et al. (2016) employed the SOLWEIG model to simulate the radiant heat flux densities in several urban settings in Shanghai, which showed good agreement with the six directional radiant flux density measurements. Research on more land cover types and the exact contribution of reflection on the radiant heat flux are required.

In the field of solar radiation measurement studies have been carried out using novel combinations of sensors to better resolve sky radiation as demonstrated in published work (Blum et al., 2022). Here a precise pyranometer was combined with a sky imager to improve the resolution of the precise data from the pyranometer. These sky imagers are inherently limited in their accuracy due to their use of a CMOS sensor which does not respond proportionally to Wm^{-2} of irradiance because of their limited spectral response.

Objective

The objective of this paper was to address some of the limitations of the initial collaboration combining the MaRTy, SMaRT, and ray tracing simulations (Aviv et al., 2021), and to carry out a more extensive field campaign to test and demonstrate improvements to the methods. A significant limitation in the first study was the inability of the SMaRT sensor to resolve any shortwave radiation as well as to record high resolution longwave scans in a short enough time period for the 1-day campaign, which resulted in significantly lower resolution images.

This study uses an updated version of the SMaRT sensor, the SMaRT Shortwave and Longwave (SMaRT-SL) that records 360° shortwave and longwave panoramic images, which is deployed alongside the MaRTy cart across locations at ASU in Tempe, Arizona for two hot clear days. It uses an updated modeling technique to better address shortwave sky radiation as well as reflections. We aimed to produce results that help better characterize through measurement and modeling the relevance of both the diffuse shortwave reflections along with the longwave emissions at a high geometric resolution. We hope this will provide a more clear picture of how the built environment, and its planned and designed landscapes and buildings, have easily-overlooked radiant relationships to the heat experienced by urban dwellers.

Measuring radiant heat transfer is critical to understanding urban heat, yet this highly variable phenomenon remains often unexamined and underappreciated in its role affecting people. Improving characterization of this phenomenon and moreover, making new tools and techniques more available to urban planners, designers, and architects will create new opportunities to better address challenges of urban heat. We argue these exchanges have many nuances including highly complex and variable heat impacts on people as they move through the geometry of the urban fabric.

METHODOLOGY

Experimental Setup and Locations

Experiments were carried out on May 18 and 19, 2021 on the ASU campus in Tempe Arizona. On each day the MaRTy cart and SMaRT-SL sensor platforms were set up at different locations in ∼2 h increments between 8:00 am and 5:30 pm. Readings were recorded from each device, panoramic photos (see **Figure 1**) were taken of the sites, and the albedo and emissivity of the surfaces were estimated.

There were five sites tested (see **Figure 1**). These varied in conditions from grass to concrete with varying levels of sky exposure. These were selected to try to achieve a variety of representative scenarios with varying sky, sun, horizon, ground cover, and ground temperature. The five sites were tested across 2 days. One site was measured on both days to have a reference (Hayden Lawn).

First, the SMaRT-SL sensor took one complete measurement which took ∼16–17 min to complete. Second, MaRTy is placed at the same location and measures for ∼1 min which includes 20 s to account for the sensor lag of the net radiometers and temperature sensor. Deploying and measuring with both MaRTy cart and SMaRT-SL sensor requires just below 20 min per location. Measuring three locations requires ∼1 h including the walk between locations.

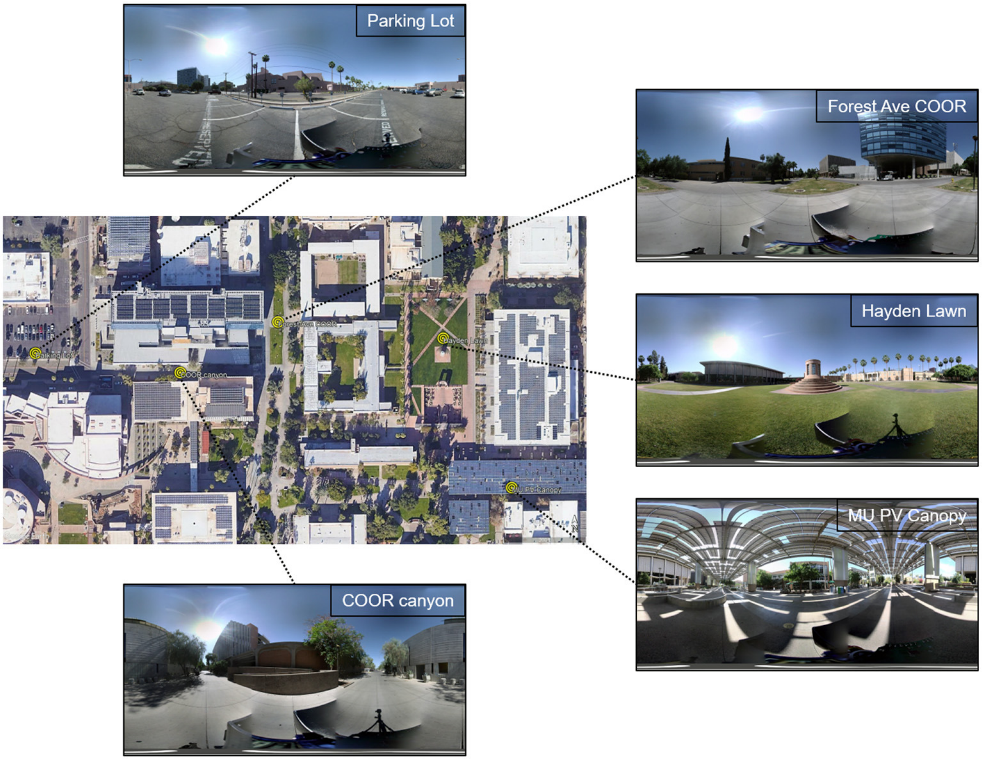

FIGURE 1 | Experiment locations on ASU Tempe campus. Panorama images of each location showing the surroundings and different conditions.

On the first day, May 18th, the sensors were deployed in three locations (1) The Hayden Lawn, a large open grass field, (2) The MU PV Canopy, an outdoor seating area under a large PV shade structure; (3) The Forest Ave COOR, a concrete open area in front of the Lattie F. Coor Hall at ASU. Five measurements were made at Hayden lawn, Six at the MUPV Canopy, and four measurements were made at Forest Ave COOR all spaced ∼2 h apart with the Hayden and MU PV starting between 8 and 9 am with the MU PV having an additional data collection between 9 and 10 am due to data loss between 8 and 9 am.

On the second day, May 19th, the sensors were rotated through three locations, again (1) Hayden Lawn (reference location), (2) Parking lot, an open area dominated by asphalt concrete, and (3) COOR canyon, a concrete walkway between buildings near the Coor Hall.

MaRTy Cart Mobile Net Radiometer Platform

The MaRTy cart setup is the same as described in our previous collaboration (Aviv et al., 2021), and as detailed in a first experiment at ASU in Tempe (Middel and Krayenhoff, 2019). It is a human-biometeorological platform (**Figure 2**), which was custom-built to be a mobile platform that is easily moved from location to location.

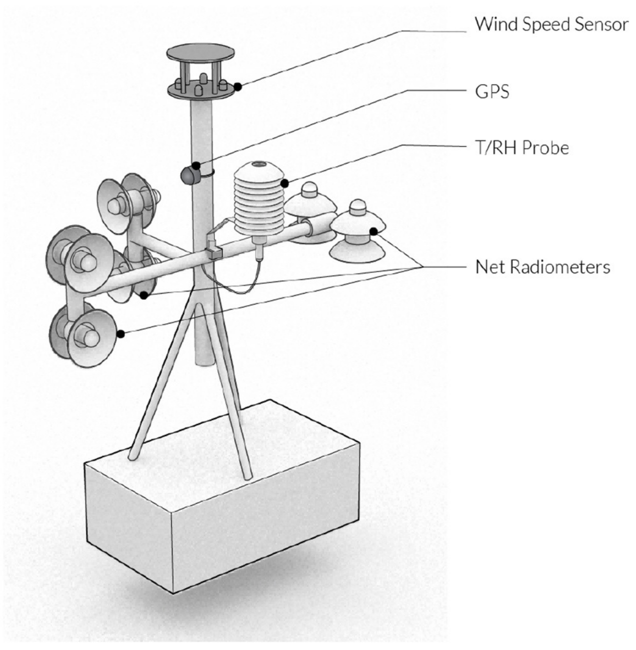

FIGURE 2 | The MaRTy cart sensor platform.

The MaRTy sensor platform records location (lat/lon,°), air temperature (°C); relative humidity (RH%); wind speed ($m{\cdot}s^{-1}$); longwave (Wm^{-2}) and shortwave (Wm^{-2}) radiant flux densities in a 6-directional Hukseflux NR-01 net radiometer setup. It determines MRT from combining net radiometer readings of directional shortwave and longwave radiation, weighting each direction according to angular factors of a standing person as per

TABLE 1 | Apogee sensor specifications.

	SL-510 Pyrgeometer	SP-510 Pyranometer
Calibration uncertainty	5%	5%
Measurement repeatability	<1%	1%
Long-term drift	<2% per year	<2% per year
Non-linearity	<1%	<1%
Spectral range	5–30 µm	385–2,105 nm
Temperature response	<5% from −15 to 45 C	<5% from −15–45 C
Window heating offset	<10 W*m^{-2}	<2 W·m^{-2}
Uncertainty in daily total	5%	5%

Equation 1:

$$T_{MRT} = \sqrt[4]{\frac{\sum_{i=1}^{6} W_i\,(a_k K_i + a_i L_i)}{a_l * \sigma} - 273.15K} \qquad (1)$$

where $a_k = 0.70$ and $a_i = 0.97$ are the unitless absorption coefficients for short-wave and longwave radiant flux densities, σ is the Stefan-Boltzmann constant in $Wm^{-2}\ K^{-4}$, and the unitless angular weighting factors of $W_i = 0.06$ for the up and down facing sensors and $W_i = 0.22$ for the sensors pointing in each cardinal direction.

SMaRT-SL Short and Longwave Mapping

We build on previous work developing a scanning mean radiant temperature sensor (SMaRT) sensor. The new expanded version includes short and longwave (SMaRT-SL) thermopile array detectors. It is composed of four directional radiative energy sensors mounted on a 2-axis rotation stage, capable of 360 degrees of motion in the azimuthal direction and 180 degrees of motion in elevation for on-demand full spherical coverage of all four sensors. In this implementation, servos are used to drive reduction gears on each rotation stage, allowing for high directional accuracy and power and communication cable pass-throughs inside the centers of the reduction gears. The system is controlled by an Arduino DUE microcontroller.

The sensor package consists of: an Apogee Instruments SP-510 Thermopile pyranometer, an Apogee Instruments SL-510 pyrgeometer, a Heimann HTPA 80x64d R2 L10.5/0.95 F7.7HiC thermopile array thermal camera, and a novel custom-made thermopile array shortwave camera using a HTPA 80x64d R2 L0 FCaF2 thermopile sensor. The novel addition of this shortwave (here meaning UV to SWIR sensitivity) thermopile camera to the conventional longwave IR thermal camera allows for explicit directional and spatial quantification of all significant radiative components of thermal comfort. The single-value pyranometer and pyrgeometer measurements are then used as comparative reference signals, and the pyranometer was additionally used for initial calibration of the sensitivity coefficient of the shortwave thermopile sensor.

The Apogee Instruments pyranometer and pyrgeometer are measured using an ADS1115 16 bit precision, differential ADC with a resolution of 3.9 µV. The pyrgeometer thermistor channel is read with a standard 12-bit ADC for a resolution of 0.8 mV. The sensor specifications and errors are shown in **Table 1**.

The Heimann HTPA 80x64d R2 L10.5/0.95 F7.7HiC thermopile array has 5,120 elements, and a field of view of ∼39 by 31 degrees. The f/0.95 lens has a LWP coating with a cut-on (Tr: 5%) at 7.7 µm ± 0.3 µm. The accuracy is ±3% $|TO - TA|$ or ± 3K (whatever is larger) for object temperatures < 300°C and ambient temperatures from 5 to 50°C, and the NETD is 140 mK@1Hz.

The shortwave thermopile array sensor combines a lensless, unfiltered thermopile array with a VIS-NIR coated achromatic optical float glass lens pair. The result is a low-resolution camera with near-flat spectral response from 375 to 2500 nm. The HTPA 80x64d R2 L0 FCaF2 thermopile sensor has an ∼1 mm thick CaF2 window to seal the device, which provides nearly flat bandpass response across the 200 µm to ∼10,000 µm range. The focusing lens is a N-BAF10/N-SF5 achromatic pair with 14 mm focal length and 12.5 mm diameter for an f-number of 1.15. A VIS-NIR (400–1,000 nm) anti-reflection coating reduces glare across the primary portion of the spectrum, and has a 50% signal range from 375 to 2,650 nm. A rectangular lens hood further reduces lens flare, an on-going issue due to the strength of the direct beam sun. Finally, a servo actuated shutter-flap is used to darken the device for zeroing and calibration of thermal offsets. See **Figure 3** for a cutaway 3-D model of the shortwave sensor.

The SMaRT-SL can complete a full set of measurements over a 15 min period. Upon power up, the tripod base is used to align the sensor in the North direction. Next, the sensor rotates to the Up, North, East, South, West and Down directions, pausing at each for ∼30 s to record the Apogee Instruments Pyranometer and Pyrgeometer readings, creating a full 6-direction net radiometer measurement with only two sensors. After this 6 direction measurement is completed, the shutter is closed on the SW thermopile camera and the raw voltage outputs of the thermopile are read and averaged over ∼30 s. This provides the baseline signal level offset due to the temperature dependent longwave IR emission of the optical elements. After this calibration is run, the device begins the panoramic scan, achieving full spherical coverage from 70 images with small overlaps over about 8 min. After the panorama is completed, a followup SWIR camera calibration and 6 direction net radiometry is taken.

SMaRT-SL Sensor Image Processing

The SMaRT-SL sensor raw data, in the form of a collection of images, is post-processed to create a Lambert cylindrical equal-area projection of the full scene. This process distributes, upscales, smooths and averages the overlapping images, and also serves the important role of evenly distributing pixel data points to have equal solid-angle view factors. The image pixels are binned and spaced at integer values in a discrete uniform distribution in the horizontal and vertical dimensions in the final projection, assuring that in 3D vector space every pixel value in the projection image has an equal solid-angle view factor. A matrix of corresponding 3D vector coordinates is saved with

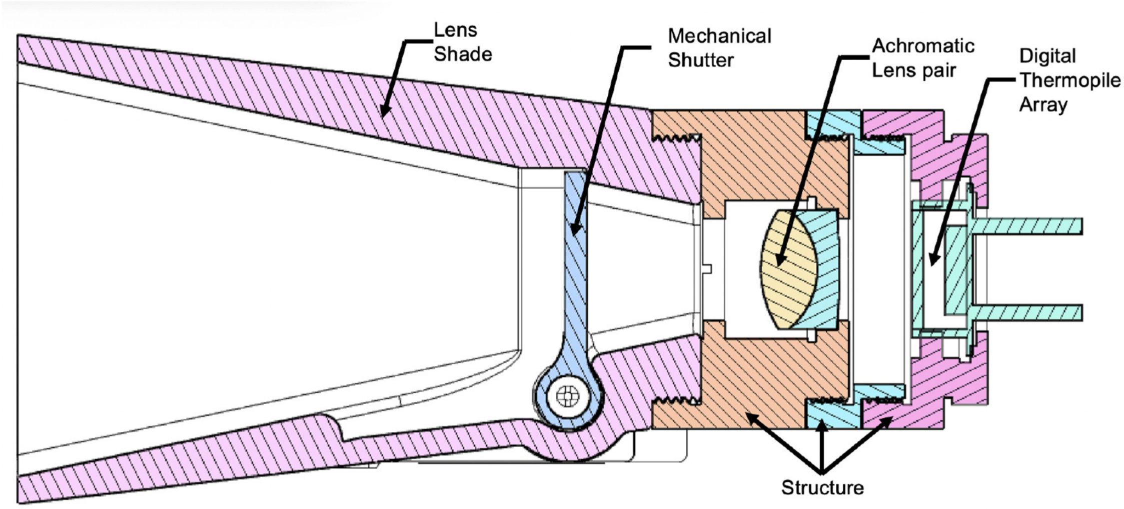

FIGURE 3 | Shortwave sensor cross section, with shutter in closed position. Adaptable system using c-mount components, and 3D printed lens shade.

the image, allowing further calculations to then be done in the projection space utilizing this even point spread.

To generate the planar irradiance values for a given direction from the SMaRT-SL data, virtual pyranometer and pyrgeometer models were used to generate singular numbers. The 3D vector coordinates of the pixels were used to apply Lambert's cosine law to weight the data points within view of the simulated plane. This allowed the generation of not only cardinal direction planar irradiance values to match the experimental pyranometer and pyrgeometer data, but of any arbitrary plane direction as well.

A further insight made possible by both the unique resolution and paired sensor setup of the SMaRT-SL allowed for very accurate classification of any given pixel in the projection of the scene as having either terrestrial, sky, or direct solar origins. This was made possible by using logic that paired the longwave and shortwave images: if the longwave reading was more than 25°C below ambient temperature the reading was classified as "sky," if the shortwave was above 1,000 $W \cdot sr^{-1} \cdot m^{-2}$ the reading was classified as "direct sun," and all other points were classified as "ground." This method proved quite robust, however further testing and refinement of the process may be required for scenes with significant cloud cover. **Figure 4** demonstrates the technique's ability to classify trees, buildings and the overall varying horizon line. This classification allows for both the quantification in any given measurement of the individual contributions of direct and reflected sources, as well as calculation of statistics such as Diffuse Horizontal Irradiance (DHI) and Direct Normal Irradiance (DNI).

FIGURE 4 | Demonstration of pixel categorization at Hayden Lawn on summed longwave and shortwave irradiance image where pixels classified as "ground" are blacked out.

Simulation Methods

For shortwave irradiance simulation, a ray-tracing model was constructed using Honeybee (version 0.66), a validated environmental plugin in the Rhino/Grasshopper algorithmic 3D modeling platform. With the inputs of the location (Phoenix, USA, 33°25' N, 111°56' W), the dates and times of the experiments (8 am-4 pm, May 18th and 19th, 2021), and the direct normal irradiance and diffuse horizontal irradiance, the model firstly generates the sky matrix for each simulation case. The resolution for determining the sun's location is 1 hour. The sun path and the sun location during the experiments are shown as **Figure 5A**. The hourly global horizontal irradiance was collected in a weather station of the Arizona Meteorological Network, which is located in the central Phoenix and around 16 kilometers away from the experimental sites. However, the meteorological data does not include direct normal irradiance and diffuse horizontal irradiance. In order to estimate the aforementioned two parameters, the Typical Meteorological Years (TMY) dataset provided by ISD (US NOAA's Integrated Surface Database) contains the irradiance data and was used as reference. Based on the combination of the two sources, the estimated direct normal irradiance and diffuse horizontal irradiance were calibrated.

For the geometric modeling, the 3D model of buildings, land surfaces of different types and trees were built and the reflectivity coefficients of all surfaces were assigned based on measurements at each site after experiments with an ASD

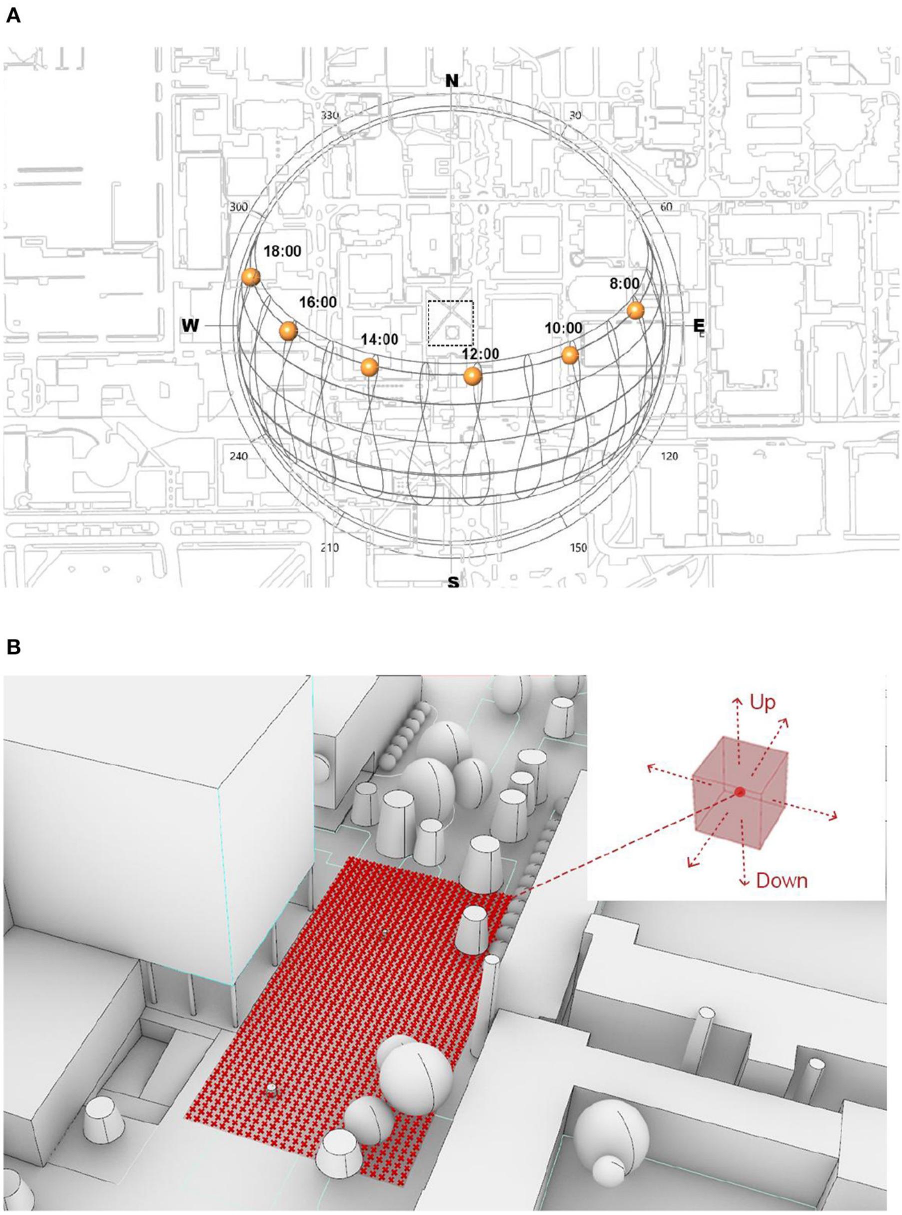

FIGURE 5 | (A) The sun path and sun locations during the measurements; **(B)** Sample points distribution of Forest Ave site.

FieldSpec 4 Spectroradiometer, with reflectivity values averaged over the 350–2,500 nm wavelength measurement range: 0.11 for asphalt ground, 0.2–0.25 for pavement, 0.5 for vegetation, 0.3 for gravel, 0.4 for photovoltaic panels, 0.3 for concrete, 0.15 for brick, 0.2 for trees. For each simulation case, a spatial map showing the mean spherical irradiance variation was created with a testing plane at the height of 1.1 m above the ground representing the centroid of humans and the testing points were generated in the resolution of 1 m. Boxes centered on the testing points were separated into six surfaces for plane irradiance calculation and the results correspond to the east, west, south, north, upward and downward orientations, respectively (**Figure 5B**). Based on these inputs, the RADIANCE engine embedded in Honeybee was used to build a ray-tracing model for irradiance simulation (Ward, 1994). The plane irradiance of all testing boxes' surfaces can be calculated, based on which the mean spherical irradiance was calculated using a cubic method. This simulation technique has been developed in our previous studies (Hou et al., 2021).

In order to investigate the reflectivity of the surrounding environment and its influence on the irradiance received on the ground, a parallel set of simulations was conducted for each case with the reflectivity coefficients of all surrounding surfaces as 0 while keeping other settings unchanged. The parallel test still includes the indirect irradiance from the sky rather than from the surfaces in the built environment such as building envelopes, since the maximum number of diffuse bounces computed by the indirect calculation were four for all cases.

RESULTS

We have selected sets of results from the five locations to best illustrate the novel data that can be resolved by combining these techniques. The full datasets will be made available and submitted as data-in-brief and posted to a github repository (chaos-laboratory/Resolving-Radiant-2022-Paper-Data). We selected illustrative datasets collected from the Forest Ave site next to the COOR building, the Hayden Lawn, and the MUPV shade canopy. These provide a range of shortwave and longwave conditions that expose the role of longwave outdoors, and terrestrial sources of reflected shortwave, both of which are often assumed to be small relative to direct sky solar radiation. We show that they are not only significant, but that they have highly variable distributions that affect the heat experienced by people across short areas, and make shaded areas capable of significant heat stress.

Longwave and Shortwave Radiant Energy Spherical Panoramas

We first present the results of the longwave and shortwave high resolution scans collected by the SMaRT-SL platform. We have false-colored the images similar to thermal imaging, but in this case the gradient is representing the $W \cdot sr^{-1} \cdot m^{-2}$ coming from that direction. For each site, Forest Ave in **Figure 6**, Hayden Lawn in **Figure 7**, and MUPV in **Figure 8** we also include a visible panorama for reference to make it easier to interpret the sources and structures that appear in the radiant panoramas. Each image is a full 360 degree panorama, and the significant variation in thermal radiation is clear. In the case of Forest Ave in **Figure 6** there are images for two times, one at 11 am and one at 3 pm. The shortwave changes dramatically from 11 am to 3 pm as the sun passes behind the COOR building and creates a large shaded area. Still there remain non-insignificant sources of reflected shortwave that are of similar, and in some areas greater, than the diffuse sky intensity. The longwave image is also very interesting for Forest Ave as the building plays a significant role as a heat source as does the hot concrete on the ground. At 2 pm the shade creates an obvious reduction in shortwave, but although the longwave has reduced without the direct heating from the sun on the surfaces, it still represents a significantly high source of radiant heat, and in the case of the building, it is blocking what would otherwise be thermally cool longwave sky.

The Hayden lawn data is representative of large open areas. The shortwave data again illustrates the significant reflection from the surrounding surfaces. Here the longwave component is more significant as the major shift in temperature from the grass to the concrete causes a major change in the radiant heat. The radiant heat from the grass surfaces is about 10–20% lower than the concrete surfaces. This shift in heat of going from standing on the lawn to standing on concrete would be equivalent to the air temperature changing by several degrees. The SMaRT-SL sensor data allows us to not only calculate the radiant temperature fields in main directions, but to now visualize the role that all designed surfaces in an environment play in the thermal load placed on people using the spaces.

The MUPV canopy presents one of the most interesting radiant datasets for our high resolution measurement case study. The variation of openings in the canopy and the significant heating of the panels cause unique shortwave and longwave conditions. While the overall amount of shortwave is certainly reduced by the canopy shading, there is still significant amounts of shortwave that arrives through the gaps in the canopy. This can largely be avoided by users as needed because the hot spots clearly register in the visible image, but we noted that our measurements even across a few inches could be dramatically influenced by the highly variable shadows cast by the system, and passing through the space users would still experience these small spaces of shortwave radiation as well as the reflections from them which are generally not considered heat source but nevertheless have an effect.

What is more critical and fully unseen is the added longwave heat emitted by the panels as they are heated in the sun and radiate down in the longwave. The shaded canopy actually blocks out the sky with a surface that is as hot as hot pavement. While blocking the sun is critical to mitigate shortwave, the rest of the sky acts as an important longwave radiant heat sink. The SMaRT-SL system can clearly display both the significant longwave radiant heat from the panels, and then also show how the sky's potential as a longwave radiant sink, or cooler, is also obstructed by the panels.

Longwave Directional Irradiance

Next we present the results for the longwave data resolved across principle directions for the various instruments for comparison in **Figure 9**. We acquired longwave data similar to our previous work (Aviv et al., 2021) taking readings using the standard net radiometer measurements from MaRTy. For the SMaRT-SL sensor an improved array detector enabled more rapid acquisition of high resolution longwave panoramas, which addressed one of the issues in the first collaboration with MaRTy where the SMaRT-SL scans took more than 30 min and had limited resolution. The longwave results are in **Figure 9** for data from the MaRTy cart and from the processed SMaRT-SL sensor longwave array, with the fraction from the sky and from the ground illustrated in a stacked bar. The Apogee Pyrgometer that was mounted on SMaRT-SL for additional verification did not produce accurate data, most likely due to overheating in the hot Arizona temperatures.

The longwave data shows consistently higher values for the terrestrial down direction, up to $615\,W \cdot m^{-2}$ for the ground on Forest Ave, and the sky in the up direction has lower values as expected, at $366\,W \cdot m^{-2}$ for the sky on Forest Ave. This MUPV canopy significantly increases the up directions longwave irradiance due to the high temperature PV panel canopy. So while providing shade, the PV canopy actually has the highest longwave heat impact in the scene. One can also see temporally the effect of the Forest Ave COOR building shading the ground in the

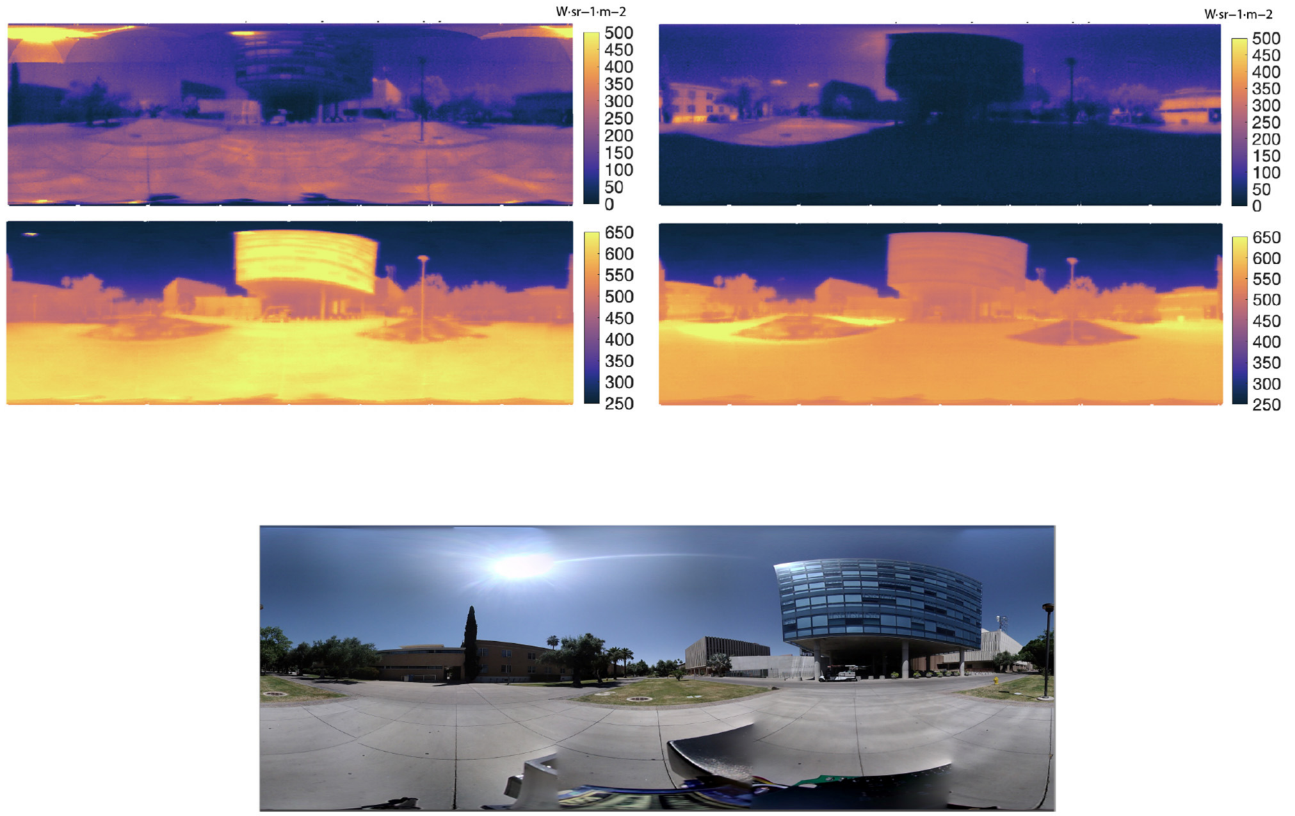

FIGURE 6 | Forest Ave Shortwave 0.3–3 μm (top) and Longwave 7.7–20 μm (middle) panorama at 11 am from the SMaRT-SL sensor scan, (right) 11 am scan and (left) 3 pm scan (bottom). Visual panorama at 11 am showing the COOR building and mixture of concrete and grass surfaces. Lambert cylindrical equal area projection used.

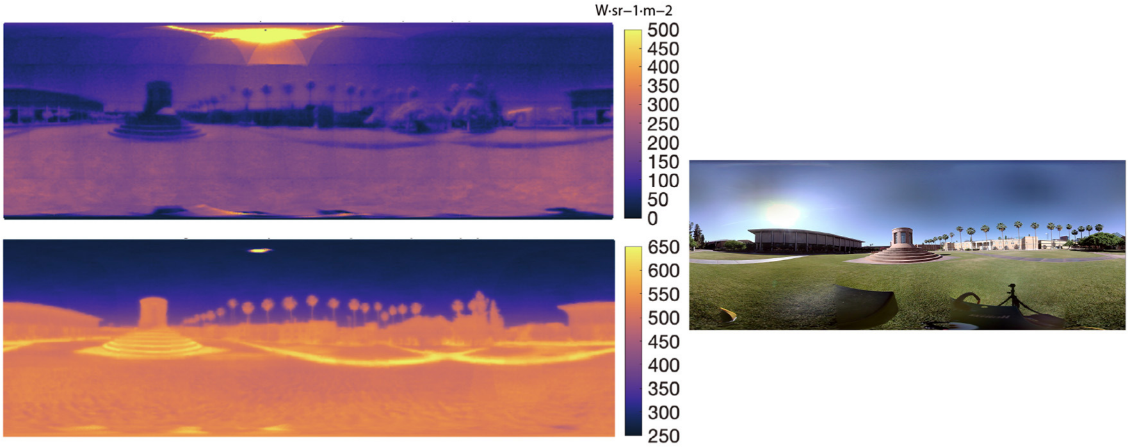

FIGURE 7 | (left) Hayden lawn Shortwave (top) and Longwave (bottom) radiant energy panorama at 2 pm from the SMaRT-SL sensor scan. (right) Hayden lawn visible panorama photo at 10 am, showing grass surfaces, sidewalks, and concrete buildings. Lambert cylindrical equal area projection used.

afternoon causing a reduction in the longwave, while similarly to the MUPV canopy causing increased longwave in the UP direction due to the presence of the hot building and reduced view to the cooler sky.

There is good agreement between the MaRTy and SMaRT-SL data, with the biggest discrepancy coming from the up direction where the significant sky portion may not be read with the same spectral sensitivity by the detectors due to filter cutoffs of the

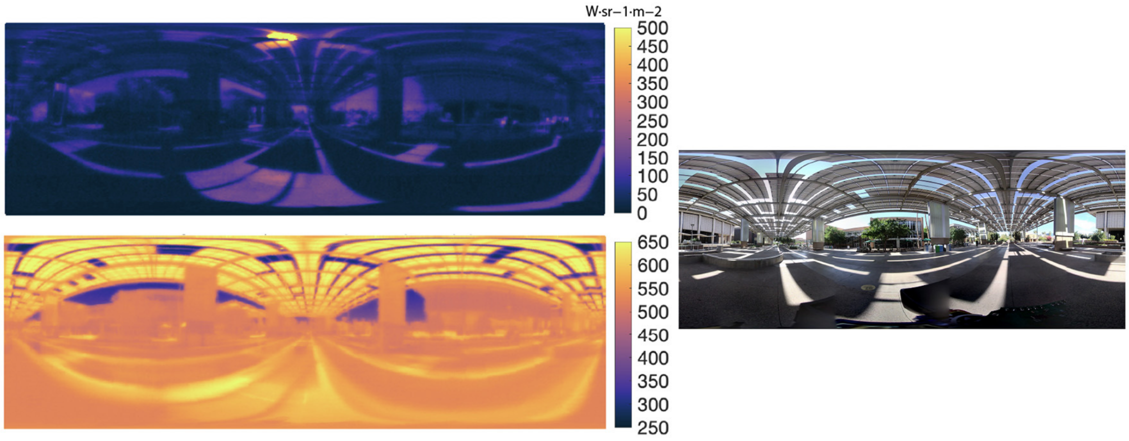

FIGURE 8 | (left) MUPV canopy shortwave (top) and longwave (bottom) radiant energy panorama at 2 pm from SMaRT-SL sensor scan, showing the significant longwave heat. (right) MUPV canopy visible panorama photo at 10 am. Lambert cylindrical equal area projection used.

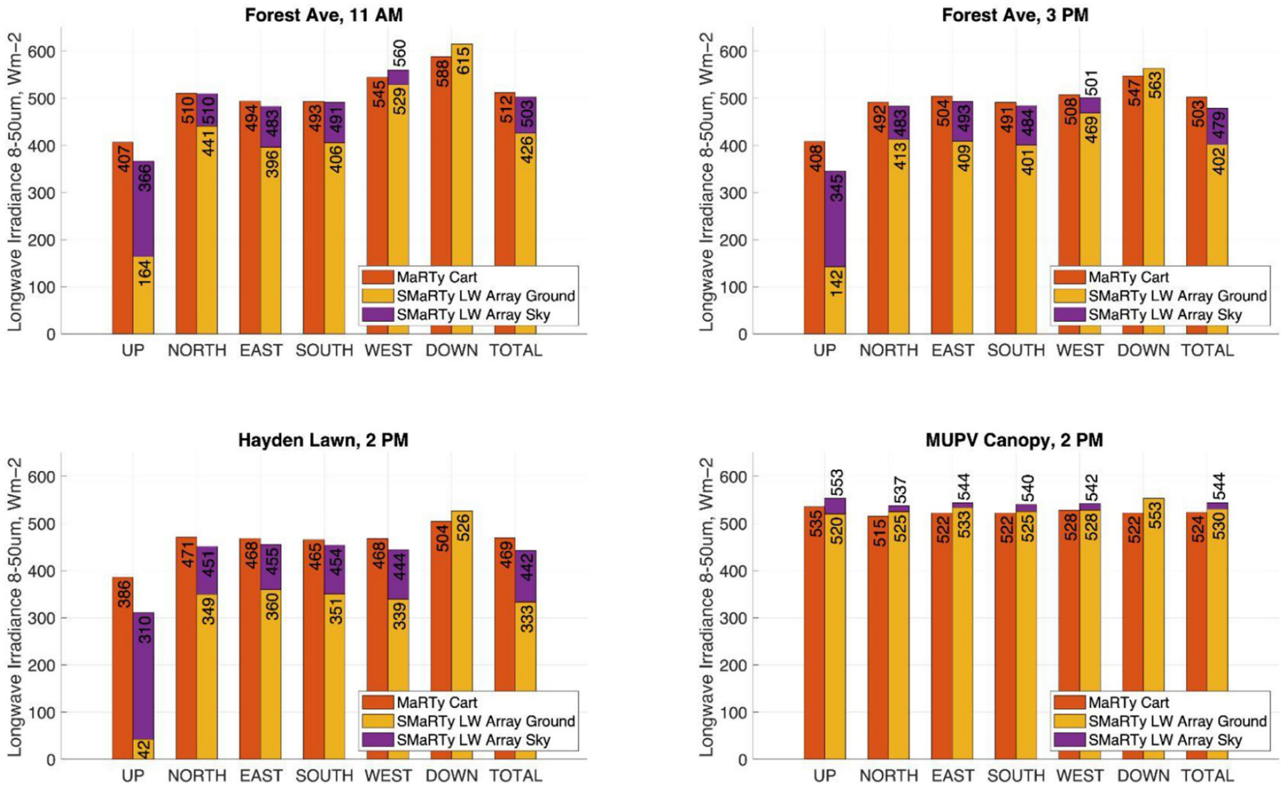

FIGURE 9 | Longwave radiation, W · m^{-2}, measured at 11 am and 3 pm at Forest Ave by the COOR, and at 2 pm at the Hayden Lawn and at the MUPV Canopy. Planar Irradiance values are from each direction and the overall average, from the MaRTy cart (left bar) and the SMaRT-SL array (right bar). The SMaRT data is broken into sky and ground components by utilizing its greater degree of resolution.

longwave sensors components, as well as differing error modes such as self heating. Generally an increased sky fraction caused the SMaRT-SL reading to be reduced compared to the MaRTy reading. Still, the results are a significant improvement over our previous work with the two systems (Aviv et al., 2021).

Shortwave Directional and Total Irradiance

The shortwave imaging data present another important extension from our previous work. The results of the new SMaRT-SL shortwave array sensor also show relatively good agreement for Forest Ave at 10 am and Hayden lawn at 2 pm as shown in

Figure 10. In this case we also have additional comparative data from the Apogee Pyrometer mounted on SMaRT-SL and from the shortwave simulation carried out to compare results from the SMaRT-SL array broken down into sky and reflected surfaces. The Forest Ave 3 pm and MUPV data are both shown on different scales because there was not direct sunlight, and in particular that limited the shortwave intensity for the Forest Ave 3 pm data. It has a maximum of just over $100\,\mathrm{W}\cdot\mathrm{m}^{-2}$, but in the morning in the sun it was nearly $1{,}000\,\mathrm{W}\cdot\mathrm{m}^{-2}$ in the upward sky direction. The MUPV data illustrates the intense local variations possible due to the PV panel shading—small differences in the physical size and location of the sensors yields highly variable results. Hayden Lawn illustrates how the reflected portion is both dominating and significant in the north and east directions—due the clear skies, the diffuse shortwave radiation from the sky is quite low. The comparison of Forest Ave at 11 am and 3 pm shows the significant differences of shading. On Forest Ave the sun went behind the building at 3 pm. both in the upwards and downwards directions, with a further marked change of the reflected portions in the cardinal directions dominating the overall radiative load. The variation among the data at Forest Ave at 3 pm is likely due to the increased difficulty of parsing out the much lower overall signals from an accurate accounting of the roughly $450\,\mathrm{W}\cdot\mathrm{m}^{-2}$ incident on the thermopile sensors due to the radiant temperature of the longwave-emitting, shortwave transparent lens system. A similar error mode can be found in low intensity pyranometer measurements.

A significant conclusion borne out by both the simulation and the SMaRT-SL sensor data is in the significance of the reflected portion of the spectrum to the overall radiative load. For the respective datasets shown in **Figure 10**, a simple accounting comparing the up and down pyranometer data shows the downwards reflected portion as 22.5, 18.2, 21, and 2.8% of the upwards direction, compared to a more accurate accounting of the ratio of the total spherical irradiance as 32.4, 45.9, 33.5, and 36.7% by an average of the SMaRT-SL and simulation data. The simple pyranometer comparison belies the significance of the reflections to the overall radiative heat transfer in lacking a more precise way of accounting for reflections. Furthermore, the accounting of reflections not just in the downwards direction holds significance for human thermal comfort, as the downwards direction has lesser impact on a standing human form (Rizzo et al., 1991).

Shortwave Reflected Radiant Heat

Figure 11 shows the variation in the fraction of reflected shortwave. Here we have data taken directly from the SMaRT-SL as well as from the simulation, which were both able to resolve shortwave arriving from the sky and direct sun as well as shortwave reflected off terrestrial surfaces. There is again relatively good agreement between simulation and the sensor. The discrepancies arise when the scene is shaded and there is more significant variation at the site of the measurement.

Improving the measurement and understanding of shortwave reflections is of particular interest because in practice the reflection of shortwave radiation off of terrestrial surfaces is often considered insignificant relative to the direct solar and sky radiation. The reflected sources of radiation ranged from 10 to 70% of the total, with the open Hayden lawn receiving a more consistent range of 25–35%. In addition, one can see both the temporal and directional dependencies of the reflected shortwave. Across the three locations, reflected shortwave was a strong component of the total radiative heat load, with certain local conditions like highly reflective buildings causing it to even become the dominant portion. By breaking the data down by direction, one can see that a simple accounting of the shortwave as simply being driven by direct radiation from the sky is highly incomplete. Furthermore, the significant variations seen in this data show the importance of more accurate and spatially resolved accountings provided by the SMaRT-SL and simulation methods to better understand the complex influences of the reflected radiative sources.

The north, south, east, and west directions provide insights into how the sun reflects off of different surfaces throughout the day, and to the high variability of heat experienced from the non-direct sources of shortwave radiation. In all cases the down direction clearly only provided reflection, but interestingly the up direction was not just direct and included reflections as well. These were caused by adjacent buildings and in particular the PV canopy site had significant reflection.

For **Figure 11A** at Forest Ave, the mean spherical irradiance keeps decreasing from 11 am (when it reaches the peak $320.4\,\mathrm{W}\cdot\mathrm{m}^{-2}$). The percentage of reflected portion in the mean spherical irradiance remains around 30%, with the highest as 32.9% at 3 pm and lowest as 26.5% at 5 pm. The avenue in the south-north direction has a high H/W ratio with buildings on both sides. Clusters of trees are on the north side. The concrete pavement and grass are reflective. From the east the reflected percentage increases and reaches the peak 83.2% ($58.1\,\mathrm{W}\cdot\mathrm{m}^{-2}$) at 3 pm, when the direct sun ray comes from the southwest direction and is reflected by the brick buildings, trees, grass and the concrete pavement. From the west the reflected percentage is high in the morning and reaches the peak 91.6% ($119.8\,\mathrm{W}\cdot\mathrm{m}^{-2}$) at 11 am, and keeps decreasing after that, when the direct sun ray comes from the southeast direction and is reflected by the building with glass facade and the concrete pavement on the west side. From the north the irradiance reaches the peak 88.0 % ($110.5\,\mathrm{W}\cdot\mathrm{m}^{-2}$) also at 11 am, and has a decreasing trend afterwards. From the south the reflection percentage decreases to the lowest at 1 pm, and increases after that. The reflection percentage at around 4 pm (∼47%) is lower than that in the lawn (51.3%) and under the PV (62.3%). For the two open sites, the reflectance of the concrete pavement in the avenue is lower than that of grass in the lawn. The space under the PV shading structure has a brick building and trees on the south side which may contribute to irradiance from the south direction through multiple bounces, resulting in a higher reflection percentage.

For **Figure 11B** at the MUPV, the Mean spherical irradiance does not fluctuate much during the day, with the highest as $89.1\,\mathrm{W}\cdot\mathrm{m}^{-2}$ at 12 pm and lowest as $56.9\,\mathrm{W}\cdot\mathrm{m}^{-2}$ at 4 pm. The percentage of reflected portion in the mean spherical irradiance does not vary much either, with the highest as 37.4% at 12 pm and lowest as 30.3% at 8 am. The irradiance from the upward direction ($224.4\,\mathrm{W}\cdot\mathrm{m}^{-2}$) is lower than that in the lawn

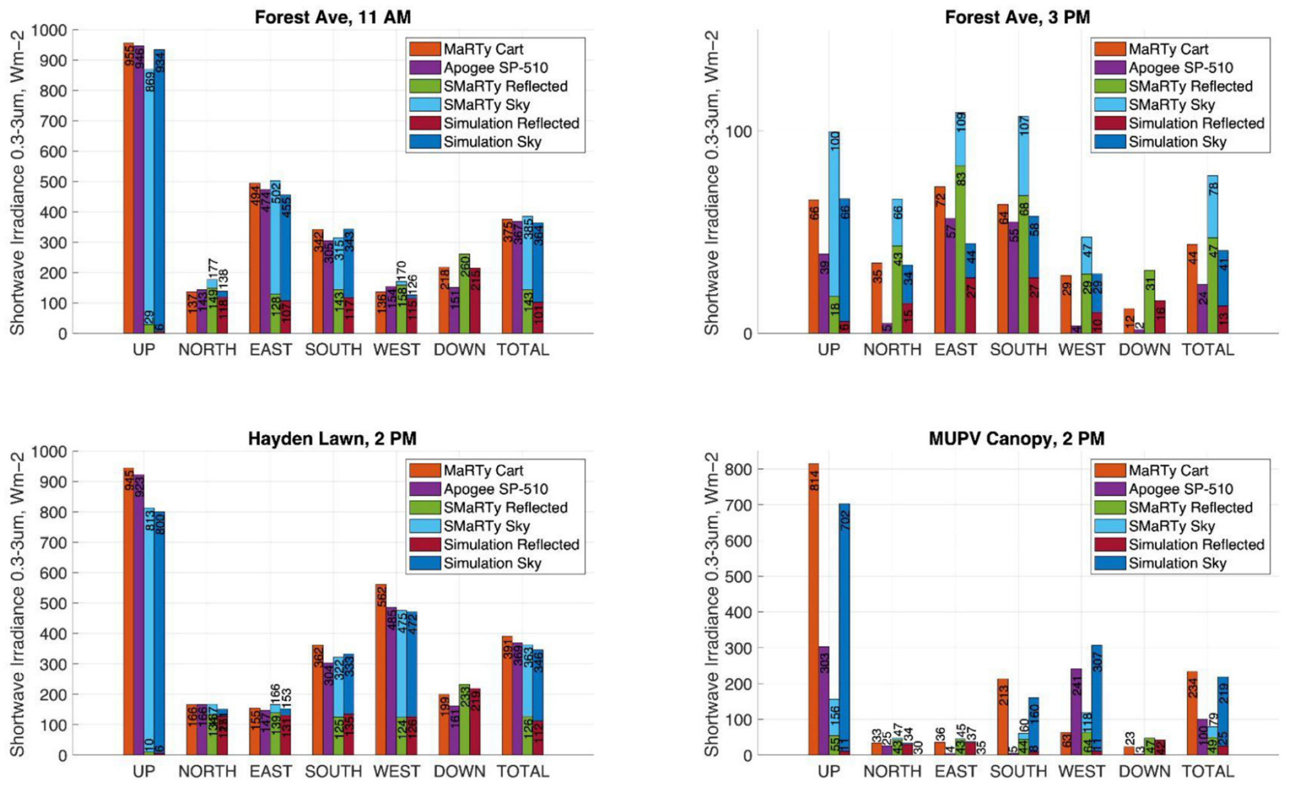

FIGURE 10 | Shortwave radiation,W · m^{-2}, measured at 11 am and 3 pm at Forest Ave by the COOR, and at 2 pm at the Hayden Lawn and at the MUPV Canopy. Planar irradiance values are from each direction and the overall average, from the MaRTy cart (left bar), the Apogee Pyranometer (middle-left bar), SMaRT array (middle-right bar), and the simulation data (right bar). The SMaRT-SL and simulation data are broken into direct sky and reflected ground components by utilizing their greater degree of resolution.

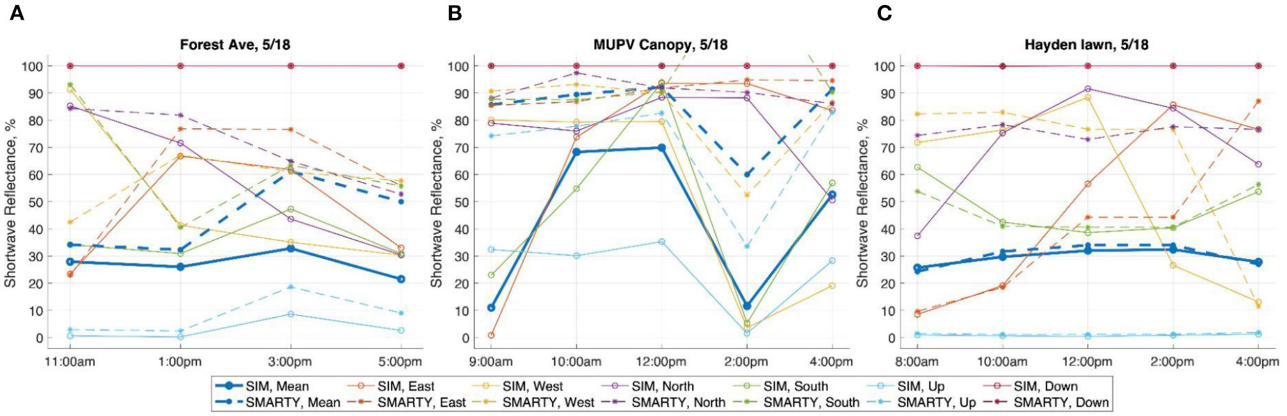

FIGURE 11 | Reflected shortwave variation across time and planar direction at Forest Ave **(A)**, MUPV **(B)**, and Hayden Lawn **(C)**. Solid lines are produced from the simulation data, and dashed lines are produced from the ratio of reflected ground to direct sky measurements taken from the SMaRT-SL sensor.

(797.6 W · m $^{-2}$) without shade above. Because of the PV panels shading above with only some gaps between panels allowing direct sunlight, the shortwave irradiance received from every direction is lower than that in the open space such as the lawn. From the east direction the reflected percentage increases from 8 am and reaches the peak 87.6% (30.8 W · m $^{-2}$) at 2 pm, when the direct sun ray comes from the southwest direction and is reflected by the columns made of brick and semi-transparent glass and the pavement. From the west the reflected percentage is high in the morning and reaches the peak 91.9% (35.3 W · m $^{-2}$) at 12 pm, and the irradiance from the north direction is relatively high and reaches the peak 94.2% (41.5 W · m $^{-2}$) also at 12 pm, when the

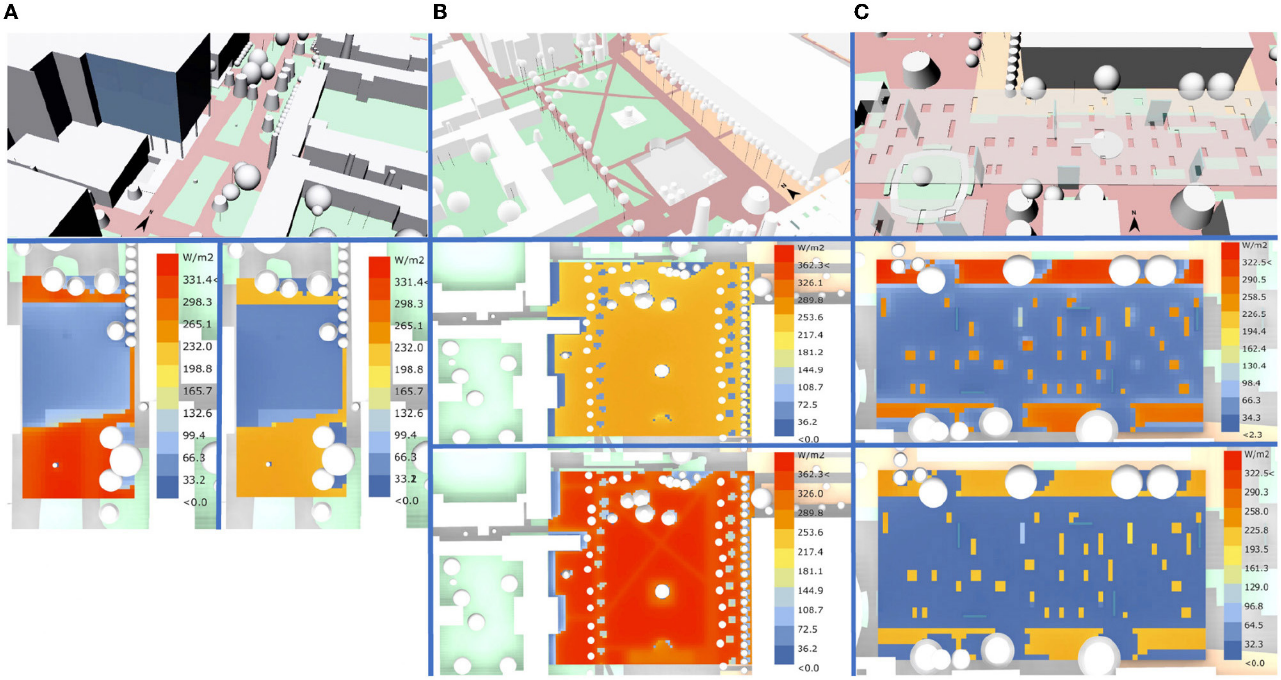

FIGURE 12 | [**(A)**, left] Simulated mean spherical irradiance map of Forest Ave site using modeled site geometry (top) simulating with interreflections (left) or without (right) surrounding interreflections at 3 pm, May 18. [**(B)**, middle] Simulated from local geometry (top) of mean spherical irradiance map for Hayden Lawn with (left) or without (right) surrounding interreflections at Hayden Lawn at 10 am on May 18. [**(C)**, right] Simulation using geometry of MUPV site (top) showing mean spherical irradiance map with (left) or without (right) surrounding interreflections at 12 pm, May 18.

direct sun ray comes from the south direction and is reflected by the brick building, trees and the pavement on the north side. The canyon in the west-east direction has a larger height-to-width ratio, which results in higher reflection percentage for the north direction. The South reflection percentage decreases from 8 am and reaches the lowest at 12 pm, and increases after that. It is around 40–60% with more direct rays received and mainly reflected from the pavement.

For **Figure 11C** at Hayden Lawn the mean spherical irradiance reaches the highest at around 12 pm. The irradiance coming from the up direction makes the largest contribution. The second highest is from the south direction in compliance with the direct sunlight direction. The reflected portion reaches the highest as 33% at around 12–2 pm. For the east direction the reflected percentage increases from 8 am and reaches the peak 86.6% (107 $W \cdot m^{-2}$) at 2 pm, when the direct sun ray comes from the southwest direction and is reflected by the brick building, trees and grass on the east side. For the west direction it is high in the morning and reaches the peak 89.9% (119.8 $W \cdot m^{-2}$) at around 10am-12pm, when the direct sun ray comes from the southeast direction and is reflected by the brick building, grass on the west side. From the north it is high at 10 am - 2 pm with the peak over 90%, when the direct sun ray comes from the southeast/south/southwest direction and is reflected by the trees on the north side. From the south there are less obstacles for the direct sunlight from the south direction, the reflection percentage is around 40–60%, mainly reflected from the grass.

TABLE 2 | Height-to-width ratio.

H/W	Lawn	MUPV	Forest Avenue	COOR	Parking lot
East	0.19	/	0.23	/	0.07
West	0.1	/	1.1	/	0.04
North	/	0.38	/	0.8	0.1
South	/	0.39	/	0.4/2.1	0.5

Simulation of Radiant Heat Variation Reflection Contribution

A further ability of the simulation method is to create 2D spatial heat maps of the total spherical Irradiance across a site as shown in **Figure 12**. These maps provide useful context for the reflected shortwave data points shown prior. One can see both the significant difference in intensity between just the direct incident radiation compared to a full accounting with reflections. The reflected portion can also be clearly seen as a strong driver of increased spatial variation in the overall Irradiance across the site.

Reflection and Geometry Comparison Between All Sites

Table 2 provides an overview of the geometry of the site related to the height of surrounding infrastructure, terrain, or plants for all sites in the four horizontal directions. **Table 3** gives the average reflected fraction of shortwave radiation for every site.

TABLE 3 | Average of reflection.

	Lawn	MUPV	Forest avenue	COOR	Parking lot
Mean Spherical	31.4%	**34.5%**	30.5%	25.9%	18.1%
East	59.2%	61.1%	61.3%	**63.7%**	57.4%
West	51.7%	**54.1%**	41.6%	39.4%	28.7%
North	79.8%	**83.1%**	70.0%	77.9%	56.4%
South	41.3%	**44.9%**	41.5%	39.7%	34.8%
Up	1.6%	**6.9%**	2.8%	4.0%	1.1%
Down	99.9%	100.0%	100.0%	100.0%	99.9%

The bold values indicate the highest reflected percentage for a given direction across the different sites.

A summary of the overall results of the reflections across all sites is as follows:

- Open spaces such as the Parking Lot have a relatively low percentage, while the Lawn has a high percentage because of reflected radiation, the grass.
- For the other three sites in urban canyons, the shading structure increases the reflection percentage of MUPV, while its H/W ratio is lower than that of Forest Avenue and COOR.
- Forest Avenue has a high average reflection percentage in the East direction, due to the concrete facade of the buildings on the east side next to the reflective ground.
- MUPV has the highest reflection percentage in general, however the mean spherical irradiance is the lowest during the day among all sites, which is attributed to the PV panels shading above with only some gaps between panels allowing direct sunlight.
- The reflection percentage of COOR is high especially in the East direction, because the concrete facade of the building on the north side contributes much to the reflection especially when the sun ray comes in from the South direction. Even though the average reflection percentage of COOR in each direction is not always the highest, its peak during the day is always higher than that of other sites. Since there is less surface facing East or West, the reflection percentage is not always high during the day, resulting in the not so high average.

DISCUSSION AND FUTURE WORK

As compared to the recent work evaluating longwave (Vanos et al., 2021), we have shown an alternative method to resolve longwave radiation with a thermopile array system using moderate cost sensors that are not sensitive to convection as with analog devices such as black globe thermometers. Comparing the recent work combining pyrometer data with sky imaging (Blum et al., 2022), we have shown an alternative method using a custom shortwave thermopile sensor that unlike a standard CMOS camera sensor provides an accurate and full spectrum measurement of the shortwave irradiance. We have validated both the longwave and shortwave systems against simulation with results from a precise pyrometer and pygometer net radiometer setup. Compared to a typical globe thermometer whose ISO 7726 standard even recognizes that convective flows around the analog device don't allow measurement better than ± 2°C, the systems we demonstrate can all produce radiant temperature values independent of convection with results within 1°C of each other across the platforms tested.

The principle set of results produced from the experiments is a set of data on the $W \cdot m^{-2}$ of irradiance in both shortwave and longwave from two different sensor platforms and a simulation. In contrast to many studies on radiant heat, we do not focus on translating this into a proxy of Meat Radiant Temperature. While we recognize the importance of temperature proxy to interpret heat, the directional and geometric nature of radiant heat transfer is actually lost when using a temperature proxy that leads most to an association with air temperature. The $W \cdot m^{-2}$ coming from each direction represent important drivers of sensation from radiant asymmetry, and the overall $W \cdot m^{-2}$ has a more direct relationship to view factor and surface area, which are both aspects of radiant heat transfer that can be acted upon by urban designers for the case of surface sizes, and also something that urban dwellers can act upon by being either informed or guided by program to areas where the less direct sources of radiant heat like reflected shortwave and infrared longwave can be minimized.

One challenge of presenting radiant results as $W \cdot m^{-2}$ is that since all surfaces are emitting, the positive values for surfaces like the sky or cooler plants are counterintuitive. They are emitting watts, but cooling because their emission is less than the temperature of the receiving human body. In our analysis we intentionally left out the temperature of the receiver. In the case of the human body, the temperature is in the range of 30 °C, and thus it is itself emitting on the order of $500\,W \cdot m^{-2}$. It is the net negative exchange with cooler surfaces that makes them cold. But this analysis of net exchange can lead to a focus on the longwave exchanges and MRT analysis that are typically done for indoor thermal comfort in buildings. We argue that both indoors and outdoors an independent accounting of the spatially resolved shortwave and longwave radiant heat can provide more specific and actionable information about how the surrounding surfaces are imparting Watts of heat upon a location. For example, in the case of the PV canopy, the total spherical longwave Watts arriving at a point below the panels has about double the heat being delivered in the longwave emission from the hot PV panels above than what would be delivered by the cool and clear sky hidden behind them, but still only about half of what the unshaded direct sun in the shortwave would be. However, rather than diminishing the effect of the longwave heating of the panels, this further begs the question of whether the geometry of the shading structure could have had less random and more strategic placement of holes to both shade from the direct path of the sun path while exposing more clear sky to cool in the longwave. In future work, we hope to use these tools of analysis to make more informed physical design and urban planning decisions based not just on average temperature proxies, but informed by a highly resolved understanding of radiant fluxes.

As we have mentioned, we neglect the temperature of the person, but that can be simply added in to estimate the net exchanges. What must also be recognized is the significance of the form of the person or other radiant receiver. The directional results are all for planar radiant fluxes, and our total results are for a spherical source receiving radiation from all directions. In other work indoors we have modeled the human body (Aviv et al., 2022*)*, and we are working to better integrate the geometry of the human body as it is inserted into these complex radiant fields. With modern computing power it is possible to use the ray tracing techniques used to simulate reflections to include net interactions with more complex geometries of the actual person who may experience heat stress or significant discomfort due to localized heating of different body parts, and the higher resolution data provided by the SMaRT-SL is critical to the use these techniques which better account for the human form.

While our aim was to study the significance of shortwave reflections, we have also shown the significance of reflections in the longwave as well (Aviv et al., 2022). These become even more complex though because surface emissivity and reflectivity in the longwave can be even more difficult to evaluate. Still, reflections in the longwave offer yet another opportunity to engage with radiant heat.

Lastly, all of this analysis is inherently dependent on an understanding of the surface and sky properties. This includes shortwave reflectivities that were estimated, but also longwave emissivities. There are also some spectral effects that may not be accurately captured where black or greybody assumptions are made. We believe in future iterations of the SMaRT-SL we will be able to use the scanning of surfaces to not only capture radiant heat fluxes from resolved surfaces, but to also capture surface types and evaluate the emissivity and reflectivity of surfaces *in situ*. This would then feed forward to allow simulations to be done quickly to determine the radiant flux at any point in space while accurately accounting for all reflections with measured material properties.

CONCLUSION

We have demonstrated a new method to improve how radiant heat transfer is resolved in both the shortwave and longwave spectral domains. It has long been recognized that the direct shortwave intense light from the sun causes significant heat, and that large warm surfaces can cause significant radiant heat in the longwave. In combination these present significant potential risk for outdoor heat stress and add to the thermal burden and energy demand of urban infrastructure.

The combination of novel tools illustrate how high precision net radiometry on a mobile platform can quickly evaluate nuances of short and longwave radiant heat variation around the hot Tempe, Arizona ASU campus, and in concert with a scanning thermopile array detector we can further resolve the precise sources of short and longwave heat across the exact geometry of the site. The high resolution data has been validated through directional averaging against the net radiometer and also for the total spherical irradiance at the measurement location with good agreement with variation ranging from 10 to 20% for values $>100\ \mathrm{W \cdot m^{-2}}$, and more significant relative difference at lower values where the internal device temperatures had a more significant impact on the relatively small measured values.

By resolving the shortwave radiation sources we can also differentiate the reflected sources from the ground vs the direct and diffuse sources from the sky. This was also validated using a simulation to consider how interreflections of shortwave contribute to the total radiant heat experienced at a location. We were able to show the sensor could accurately measure the reflected shortwave and also show that it was above 30% for three out of five sites when averaging the 4–5 measurements taken throughout the day.

In closing, we believe there is significant potential to better evaluate radiant heat fluxes as they affect urban dwellers in a variety of ways. In the future we hope these improved techniques can contribute to better characterization and ideally to exposing opportunities to better respond to the challenges presented in our ever warming urban climates.

DATA AVAILABILITY STATEMENT

The datasets presented in this study can be found in online repositories. The names of the repository/repositories and accession number(s) can be found at: https://github.com/chaos-laboratory/Resolving-Radiant-2022-Paper-Data.

AUTHOR CONTRIBUTIONS

CM, FM, MH, DA, FS, and AM planned the experiments and contributed to the interpretation of the results. FS and AM carried out the experiments and provided and operated their SMARTY cart sensor system. MH and DA planned and carried out the simulations and corresponding analysis. CM conceived and built the novel scanning array sensor SMART-LS and planned and carried out the novel analysis methods on the SMART-LS data. FM and CM took the lead in writing the manuscript, with MH providing contributions. All authors provided critical feedback and helped shape the research, analysis, and manuscript. All authors contributed to the article and approved the submitted version.

FUNDING

This study was funded in part by the US National Science Foundation's Sustainability Research Network Cooperative Agreement # 1444758.

REFERENCES

Ali-Toudert, F. (2021). Exploration of the thermal behaviour and energy balance of urban canyons in relation to their geometrical and constructive properties. *Build. Environ.* 188, 107466. doi: 10.1016/j.buildenv.2020.107466

Aviv, D., Gros, J., Alsaad, H., Teitelbaum, E., Voelker, C., Pantelic, J., et al. (2022). A data-driven ray tracing simulation for mean radiant temperature and spatial variations in the indoor radiant field with experimental validation. *Energy Buildings.* 254, 111585. doi: 10.1016/j.enbuild.2021.111585

Aviv, D., Guo, H., Middel, A., and Meggers, F. (2021). Evaluating radiant heat in an outdoor urban environment: Resolving spatial and temporal variations with two sensing platforms and data-driven simulation. *Urban Climate* 35, 100745. doi: 10.1016/j.uclim.2020.100745

Aviv, D. H. (2019). "Thermal reality capture. ACADIA 19:UBIQUITY AND AUTONOMY," in *Proceedings of the 39th Annual Conference of the Association for Computer Aided Design in Architecture (ACADIA)* (Austin, TC: The University of Texas at Austin School of Architecture), 338–345. Available online at: http://papers.cumincad.org/cgi-bin/works/paper/acadia19_338

Blum, N. B., Wilbert, S., Nouri, B., Lezaca, J., Huckebrink, D., Kazantzidis, A., et al. (2022). Measurement of diffuse and plane of array irradiance by a combination of a pyranometer and an all-sky imager. *Solar Energy* 232, 232–247. doi: 10.1016/j.solener.2021.11.064

Chen, K. W., Teitelbaum, E., Meggers, F., Pantelic, J., and Rysanek, A. (2020). Exploring membrane-assisted radiant cooling for designing comfortable naturally ventilated spaces in the tropics. *Build. Res. Infm.* 49, 483–495. doi: 10.1080/09613218.2020.1847025

Chen, L., Yu, B., Yang, F., and Mayer, H. (2016). Intra-urban differences of mean radiant temperature in different urban settings in Shanghai and implications for heat stress under heat waves: a GIS-based approach. *Energy Build.* 130, 829–842. doi: 10.1016/j.enbuild.2016.09.014

Doan, Q.-V., and Kusaka, H. (2019). Development of a multilayer urban canopy model combined with a ray tracing algorithm. *SOLA* 15, 37–40. doi: 10.2151/sola.2019-008

Hoppe, H. (1992). A new procedure to determine the mean radiant temperature outdoors. *Wetter Unt Leben* 44, 147–151.

Hou, M., Pantelic, J., and Aviv, D. (2021). Spatial analysis of the impact of UVGI technology in occupied rooms using ray-tracing simulation. *Indoor Air.* 31, 1625–1638.

Houchois, N., Teitelbaum, E., Chen, K. W., Rucewicz, S., and Meggers, F. (2019). The SMART sensor: fully characterizing radiant heat transfer in the built environment. *J. Phys.s* 1343, 012073. doi: 10.1088/1742-6596/1343/1/012073

IPCC. (2021). *Summary for Policymakers. Climate Change 2021: The Physical Science Basis. Contribution of Working Group I to the Sixth Assessment Report of the Intergovernmental Panel on Climate Change*. IPCC. Available online at: https://www.ipcc.ch/report/ar6/wg1/downloads/report/IPCC_AR6_WGI_SPM_final.pdf (accessed May 30, 2022).

Johansson, E., Thorsson, S., Emmanuel, R., and Krüger, E. (2014). Instruments and methods in outdoor thermal comfort studies – the need for standardization. *Urban Climate* 10, 346–366. doi: 10.1016/j.uclim.2013.12.002

Krayenhoff, E., Christen, A., Martilli, A., and Oke, T. (2013). A multi-layer radiation model for urban neighbourhoods with trees. *Urban Climate News* 151, 139–178. doi: 10.1007/s10546-013-9883-1

Lindberg, F., and Grimmond, C. S. B. (2011). The influence of vegetation and building morphology on shadow patterns and mean radiant temperatures in urban areas: model development and evaluation. *Theor. Appl. Climatol.* 105, 311–323. doi: 10.1007/s00704-010-0382-8

Lindberg, F., Holmer, B., and Thorsson, S. (2008). SOLWEIG 1.0 – modelling spatial variations of 3D radiant fluxes and mean radiant temperature in complex urban settings. *Int. J. Biometeorol.* 52, 697–713. doi: 10.1007/s00484-008-0162-7

Lindberg, F., Onomura, S., and Grimmond, C. S. B. (2016). Influence of ground surface characteristics on the mean radiant temperature in urban areas. *Int. J. Biometeorol.* 60, 1439–1452. doi: 10.1007/s00484-016-1135-x

Meggers, F., Aschwanden, G., Teitelbaum, E., Guo, H., Salazar, L., and Bruelisauer, M. (2016). Urban cooling primary energy reduction potential: system losses caused by microclimates. *Sustai. Cities Soc.* 27, 315–323. doi: 10.1016/j.scs.2016.08.007

Middel, A., Häb, K., Brazel, A. J., Martin, C. A., and Guhathakurta, S. (2014). Impact of urban form and design on mid-afternoon microclimate in Phoenix Local Climate Zones. *Landsc. Urban Plan.* 110, 113–122. doi: 10.1016/j.landurbplan.2013.11.004

Middel, A., and Krayenhoff, E. S. (2019). Micrometeorological determinants of pedestrian thermal exposure during record-breaking heat in Tempe, Arizona: introducing the MaRTy observational platform. *Sci. Total Environ.* 687, 137–151. doi: 10.1016/j.scitotenv.2019.06.085

Oke, T. R. (1982). The energetic basis of the urban heat island. *Q. J. R. Meteorol. Soc.* 108, 1–24. doi: 10.1002/qj.49710845502

Rizzo, G., Franzitta, G., and Cannistraro, G. (1991). Algorithms for the calculation of the mean projected area factors of seated and standing persons. *Energy Build.* 17, 221–230. doi: 10.1016/0378-7788(91)90109-G

Rosado, P. J., Ban-Weiss, G., Mohegh, A., and Levinson, R. M. (2017). Influence of street setbacks on solar reflection and air cooling by reflective streets in urban canyons. *Solar Energy* 144, 144–157. doi: 10.1016/j.solener.2016.12.026

Teitelbaum, E., Alsaad, H., Aviv, D., Kim, A., Voelker, C., Meggers, F., et al. (2022). Addressing a systematic error correcting for free and mixed convection when measuring mean radiant temperature with globe thermometers. *Sci. Rep.* 12, 6473. doi: 10.1038/s41598-022-10172-5

Teitelbaum, E., Chen, K. W., Aviv, D., Bradford, K., Ruefenacht, L., Sheppard, D., et al. (2020). Membrane-assisted radiant cooling for expanding thermal comfort zones globally without air conditioning. *Proc. Nat. Acad. Sci. U.S.A.* 117:21162–21169. doi: 10.36227/techrxiv.12034971

Teitelbaum, E., Guo, H., Read, J., and Meggers, F. (2017). "Mapping comfort with the SMART (Spherical Motion Average Radiant Temperature) sensor," in *Proceedings of the 15th IBPSA Conference*. Available online at: http://www.ibpsa.org/proceedings/BS2017/BS2017_644.pdf (accessed May 30, 2022).

Teitelbaum, E., Read, J., and Meggers, F. (2016). *Spherical Motion Average Radiant Temperature Sensor(SMART Sensor). Expanding Boundaries: Systems Thinking for the Built Environment.* (Zurich).

Thorsson, S., Lindberg, F., Eliasson, I., and Holmer, B. (2007). Different methods for estimating the mean radiant temperature in an outdoor urban setting. *Int. J. Climatol.* 27, 1983–1993. doi: 10.1002/joc.1537

Vallati, A., Mauri, L., and Colucci, C. (2018). Impact of shortwave multiple reflections in an urban street canyon on building thermal energy demands. *Energy Build.* 174, 77–84. doi: 10.1016/j.enbuild.2018.06.037

Vanos, J. K., Rykaczewski, K., Middel, A., Vecellio, D. J., Brown, R. D., and Gillespie, T. J. (2021). Improved methods for estimating mean radiant temperature in hot and sunny outdoor settings. *Int. J. Biometeorol.* 65, 967–983. doi: 10.1007/s00484-021-02131-y

Ward, G. J. (1994). "The Radiance lighting simulation and rendering system," in *Proceedings of the 21st Annual Conference on Computer Graphics and Interactive Techniques.* (New York, NY). doi: 10.1145/192161.192286

Yang, X., and Li, Y. (2015). The impact of building density and building height heterogeneity on average urban albedo and street surface temperature. *Build. Environ.* 90, 146–156. doi: 10.1016/j.buildenv.2015.03.037

Conflict of Interest: CM and FM are working to potentially commercialize technology based on and related to sensors developed as part of this work.

The remaining authors declare that the research was conducted in the absence of any commercial or financial relationships that could be construed as a potential conflict of interest.